Probing molecular layers with low-energy electrons

Tebyani, A.

4

Low-Energy Electron Irradiation Damage in Few-Monolayer Pentacene Films *

Abstract

Crystalline films of pentacene molecules, 2-4 monolayers in thickness, are grown via *in situ* sublimation on silicon substrates in the ultrahigh vacuum chamber of a low energy electron microscope. It is observed that the diffraction pattern of the pentacene layers fades upon irradiation with low-energy electrons. The damage cross-section is found to increase by more than an order of magnitude for electron energies from 0 eV to 10 eV, and by another order of magnitude from 10 eV to 40 eV. Close to 0 eV, damage is virtually nil. Creation of chemically reactive atomic centers after electron attachment or impact ionization is thought to trigger chemical reactions between neighboring molecules that gradually transform the layer into a disordered carbon nanomembrane. Additionally, diminishing of spectroscopic features related to the unoccupied band structure of the layers, accompanied by loss of definition in real-space images, as well as an increase in the background intensity of diffraction images during irradiation point to chemical changes and formation of a disordered layer.

---

* This chapter has been published as "Low-Energy Electron Irradiation Damage in Few-Monolayer Pentacene Films", A. Tebyani, F.B. Baalbergen, R.M. Tromp, S.J. van der Molen, J. Phys. Chem. C 125, 26150 (2021)

4.1 Introduction

Interaction of low-energy electrons (LEEs) with organic materials is of importance in several areas of research and applications. One important example is interaction of biological matter with ionizing radiation. Regardless of the radiation source (electrons or photons), exposure leads to generation of secondary electrons with relatively low energies (below 20 eV). These electrons are responsible for a substantial part of the damage to the organic sample. [1,2] Knock-on displacement of atoms and creation of structural defects occur with electrons of much higher energies (threshold of ~86 keV for knock-on displacement in graphene [3]). Techniques such as low-energy TEM [4], cryo-electron microscopy [5–8], or encapsulation [9] are attempts to reduce the damage and to extend sample lifetime. [10] An understanding of the energy dependence of interaction of LEEs with organic samples is beneficial for designing experiments that cause less damage to the sample under study. Another key example is formed by organic Self-Assembled Monolayers (SAMs), which can be used to modify chemical, physical, and mechanical properties of surfaces. Irradiation of SAMs with LEEs can cause (desirable) chemical changes, transforming SAMs into carbon nanomembranes (CNMs) with different properties. [11–16] Hence, knowledge of the interaction of LEEs with molecules is important in designing SAMs towards the wanted functionality after exposure to LEEs. Synthesis of carbon-based (nano)materials by utilizing an electron beam is a similar application. [17–20] Another technologically important example of interaction of LEEs with organic matter is in e-beam lithography, where electrons are used to cause chemical changes in the resist film. A detailed understanding of the interaction of low-energy (secondary) electrons with the resist is essential for control over the properties of the exposed area, as well as sharpness of the written patterns and overall quality of the lithography process. Knowledge of the role of secondary electrons, which generally have low energies, is also of great importance to understand and improve extreme ultraviolet (EUV) lithography, generally considered the key lithographic technology for the next decade(s). [21,22]

In this work, we use Low-Energy Electron Microscopy (LEEM) to study the interaction of LEEs with crystalline layers of pentacene grown on a silicon (111) substrate. In LEEM, the energy of the electrons interacting with the sample can be tuned in the range 0-100 eV (with respect to the vacuum energy) with 0.25 eV energy spread. Scattering of LEEs from pentacene layers provides information about the surface structure through diffraction, and also reveals spectroscopic features related to the unoccupied band structure [23,24], as well as electronic excitations in electron energy loss spectra. [25] The pentacene layers studied, two to four monolayers in thickness, are grown *in situ* in the ultrahigh vacuum (UHV) chamber of the microscope. Growth is monitored in real-time via both LEEM and

Photo-Electron Emission Microscopy (PEEM). Not only does this offer a high degree of control over pentacene thin film growth, it also ensures that the layers are not at any point contaminated due to exposure to air. The pentacene layers are exposed to electrons with a defined energy, and the main observation reported here is fading of the pentacene diffraction intensity due to beam-induced damage to the crystalline structure. To quantify the damage, line profiles of diffraction spots are analyzed over time. We obtain electron cross-sections for destruction of the pentacene lattice for electron energies between 0 eV and 40 eV, and find that the cross-section becomes vanishingly small for electron energies close to 0 eV. Spectroscopic information on the unoccupied band structure and electron energy loss spectra were also obtained and their evolution upon irradiation was investigated.

4.2 Experimental Technique

A schematic of the LEEM instrument is shown in Fig. 4.1(a). Electrons traveling from the cold-field emission gun through the microscope column with a kinetic energy of 15 keV are deflected towards the sample by magnetic prism 1. The sample voltage is set at -15 kV + V_0 so that the electrons are decelerated just before they interact with the sample to a kinetic energy of $eV_0 + \Delta\Phi$, in an electric field of approximately 10 kV/mm. $\Delta\Phi$ represents the difference between the work functions of the sample and the electron gun. After interaction with the sample, some of the electrons are back-reflected. These electrons are re-accelerated by the same electric field towards the magnetic prism and are deflected towards the detector via an aberration-correcting path comprised of magnetic prism 2 and the correcting electron mirror optics. [26] It is possible to project either the real-space or the diffraction-space image on the detector screen. A high-pressure Hg UV lamp attached to the sample chamber allows for imaging with photoelectrons (PEEM). In addition, a Knudsen cell evaporator is connected to the sample chamber with line of sight to the sample surface. By heating the cell, pentacene (purchased from Sigma Aldrich, with a purity of 99.995%) is sublimated towards the sample for *in situ* thin film growth. The growth of pentacene layers on silicon has been explored in detail in the literature. [27–29] (see also Fig. 4.1(b-c)) By placing a slit in the beam path in a diffraction plane between the objective lens and magnetic prism, Electron Energy Loss Spectroscopy (EELS) data can be obtained. [25] Electrons with different energies are dispersed by the magnetic prism, and hence spectra showing electron intensity vs energy are observed directly on the image screen.

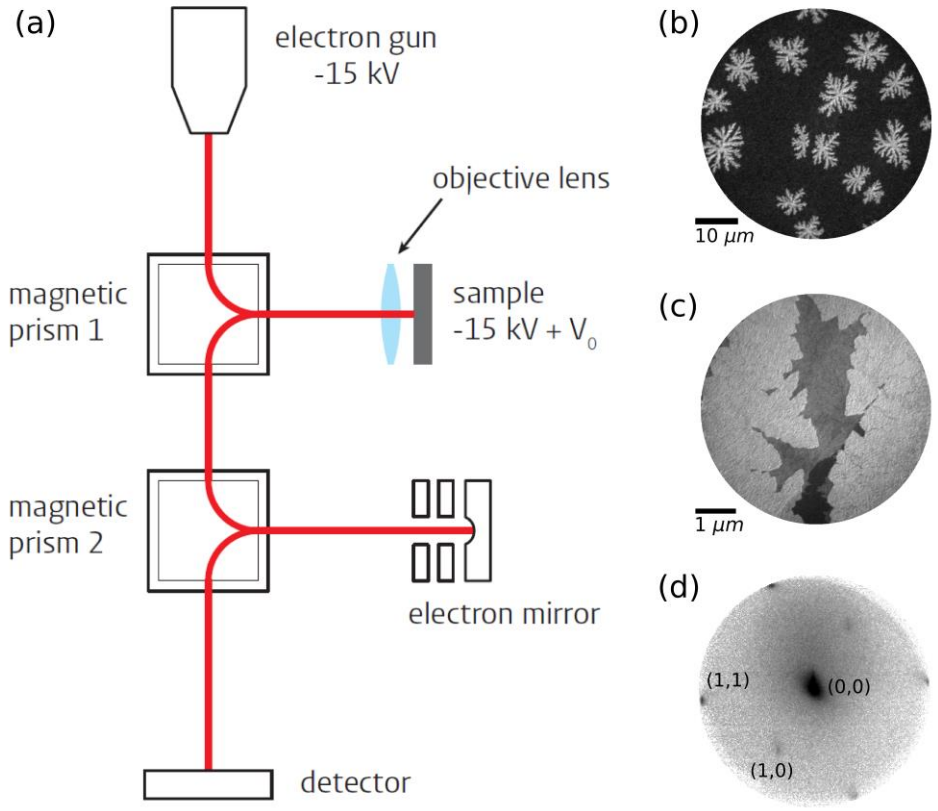

Fig. 4.1 Low-Energy Electron Microscopy (LEEM). (a) A schematic of the LEEM instrument. The red line shows the path traversed by the electrons from the cold-field emission gun to the detector. The electrons are decelerated to an energy close to 0 eV by the electric field between the objective lens and the sample, approximately 10 kV/mm in strength. The precise energy of the electrons upon interaction with the sample is tuned by V_0. The electron mirror corrects lowest-order aberrations. (b) PEEM image showing nucleation of pentacene molecules on the substrate surface and start of growth of the first pentacene layer with herringbone crystal structure (c) Bright-Field LEEM image obtained with a beam of 1.3 eV electrons. The contrast indicates different layer thickness. (d) Low-Energy Electron Diffraction (LEED) pattern of herringbone crystal structure of a pentacene film, with different diffraction orders annotated. Intensities of diffraction spots are in logarithmic scale.

Growth of the pentacene layers *in situ* in a UHV pressure of ~1.0×10^{-9} mbar and below, and keeping them in the same pressure during the entire measurements, ensures cleanliness of the surface. For obtaining the data presented here, an aperture is placed along the illuminating beam path to confine the beam to a smaller, more homogeneous area (below 2 μm in diameter) on the pentacene layer. The diffraction pattern corresponding to the chosen area is recorded over time as the layer is exposed to the electron beam. Recordings are made for

exposures to electrons with incident energies in the range 0-40 eV. The measurements are carried out at room temperature.

The total emission current of the electron gun is measured via an anode aperture that transmits about 0.1% of the emitted electrons. The ratio between the beam current that passes through this aperture and the total emission current was determined by placement of an aperture along the magnetic prism diagonal and measurement of the aperture current with a Keithley Picoammeter when the aperture blocked the beam. Electron beam current densities used are 3-45 pA/μm^2, corresponding to ~19-281 e$^-$/nm^2/sec. The surface density of pentacene molecules is about 4.74 molecules/nm^2. [29]

4.3 Results

Pentacene layers grow on silicon (111) substrates in a thin-film phase with a herringbone crystal structure (see Fig. 1.1 in chapter 1). [29] The corresponding diffraction pattern is shown in Fig. 4.1(d). In Fig. S4.1 (Supporting Information, Part A) and the inset in Fig. 4.2, we show a measurement of a typical diffraction spot and its line profile. The line profile is taken in the direction orthogonal to that of the magnetic prism dispersion (which is in vertical direction in Fig. S4.1) in order to avoid asymmetric broadening of the line profile. Next, the background is removed from the images by the following procedure: First, a Fourier transform of the diffraction image for each frame of the recording is generated. Then, a median filter is applied to the Fourier transformed image. This operation removes the low-frequency noise and the background present in the diffraction image. Finally, the filtered image is transformed back and a new diffraction image with reduced noise and background is obtained. The full process is illustrated in Fig. S4.1. Next, Lorentzian functions are fitted to the line profiles of the diffraction spots for each frame of the recording; see the inset in Fig. 4.2. To quantify the rate of fading of the diffraction pattern, we plot the amplitudes of the Lorentzian fits as a function of the cumulative electron dose (number of electrons per nm^2). Fitting an exponential function to these amplitudes yields the cross-section for damage to the pentacene crystal lattice at the incident electron energy corresponding to the recording; see Fig. 4.2. The fitted function has the form $Ae^{-\sigma \cdot D} + B$, where D is the cumulative dose in units of number of electrons per nm^2, σ is the damage cross-section in nm^2, and A and B are constants. By repeating the procedure described above for recordings corresponding to different incident electron energies, we obtain damage cross-sections as a function of electron energy. Fig. 4.3 shows the results of this analysis on diffraction peaks of different orders,

obtained from a representative sample, four pentacene monolayers in thickness. Note again that electron energies are determined with respect to the vacuum energy.

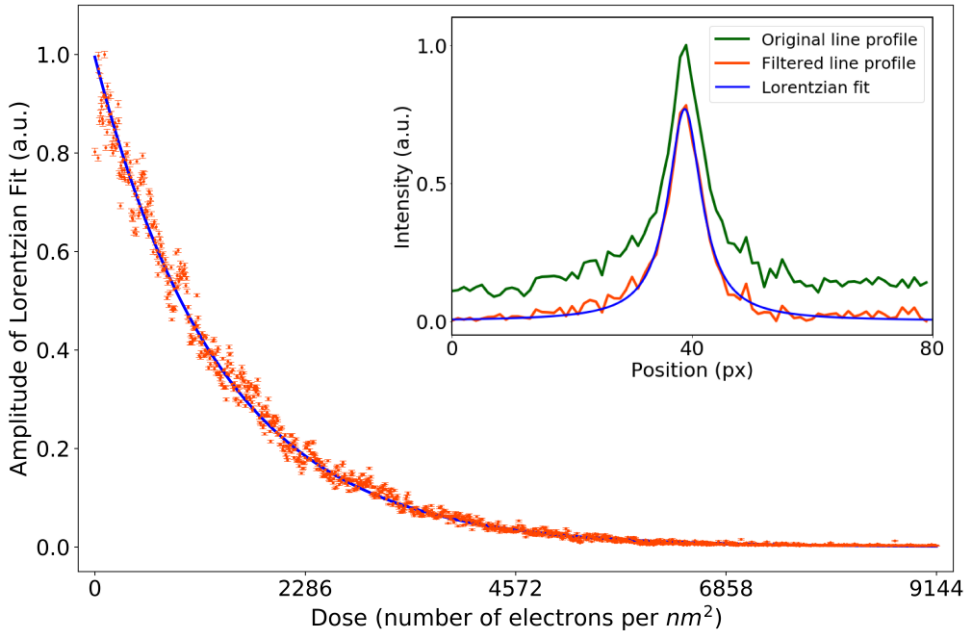

Fig. 4.2 Orange points: Amplitudes of Lorentzian fits to a (1,1) diffraction peak as a function of dose. The latter is proportional to irradiation time. Solid line: exponential fit of the form $Ae^{-\sigma \cdot dose} + B$ to the decay of the peak amplitude. A and B are constants. From the fit, we determine the damage cross-section, defined as σ in the exponent. The pentacene film is 4 monolayers thick and is irradiated with 10 eV electrons. The beam current density is 2.96 pA/μm^2. The inset shows line profile of a (1,1) diffraction peak before and after filtering, corresponding to Fig. S4.1. Lorentzian fit to the diffraction peak after filtering is also depicted.

Fig. 4.3 shows that the damage cross-section decreases sharply below 10 eV. A similar behavior is reproduced in datasets from several other samples (Figs. S4.2-S4.4, Supporting Information, Part B). For the dataset represented in Fig. 4.3, the intensity of the diffraction peaks did not decrease during the duration of the recording for electron energies below 5.5 eV. In some of the other datasets, decays were observed down to about 2 eV, with the damage cross-section becoming vanishingly small for few-eV electrons. In all cases a sharp decrease (in an almost exponential manner) in damage cross-section is observed as the energy of the incident electrons decreases below 10 eV. Changes in damage cross-section span up to two orders of magnitude for electron energies starting from the observed damage threshold for the dataset up to 10 eV. The damage cross-section increases by about another order of magnitude for electron energies between 10 eV and 40 eV, and in general shows a monotonic

behavior. Finally, damage cross-sections obtained from higher-order diffraction peaks are consistently higher than those obtained from lower-order diffraction peaks, both in Fig. 4.3 and in the results from several other samples with very few exceptions. This observation indicates that high-resolution information, i.e. short-range order, is lost before loss of order across the entire irradiated area. Faster fading of higher-order diffraction peaks has also been reported in the literature. [10,30] For completeness, Fig. S4.5 (Supporting Information, Part C) shows a typical example of changes in the width of the Lorentzian fits over time, exhibiting a generally increasing trend.

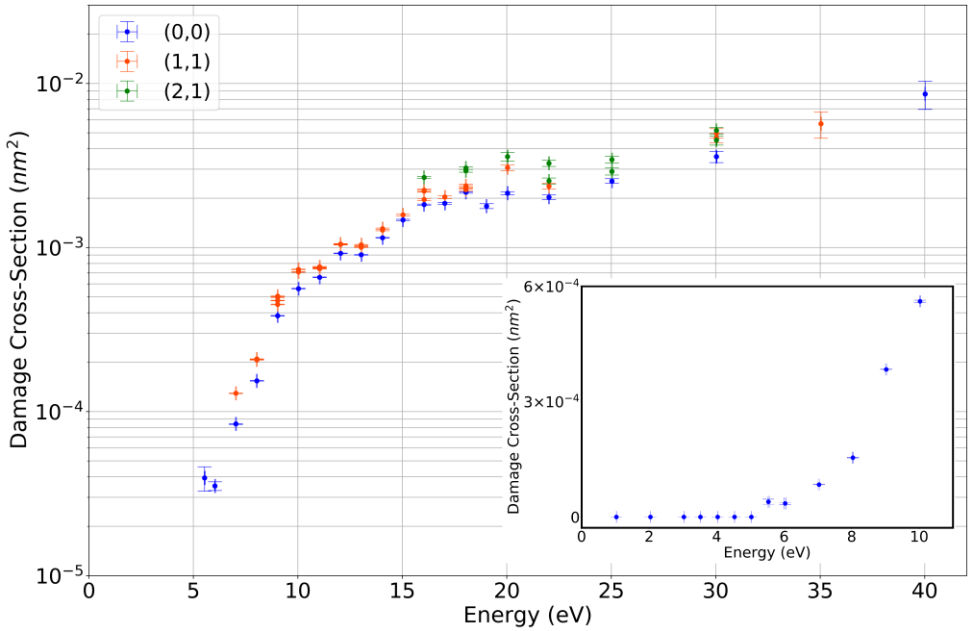

Fig. 4.3 Damage cross-sections (see Fig. 4.2) of different-order diffraction peaks versus incident electron energy for a pentacene sample with thickness of 4 monolayers. The beam current density used for obtaining the cross-sections is 2.96 pA/μm^2. The inset shows the damage cross-section for datapoints up to 10 eV in linear scale, including energies for which no decay in diffraction intensity was observed.

Changes induced in the film upon irradiation are also observed in real-space. During irradiation, the structure of the layer gradually loses definition and sharpness and becomes darker in bright-field images. To obtain bright-field images, a contrast aperture is placed around the 0th-order diffraction peak to exclude all the electrons which are not specularly reflected, including secondary electrons. After a sufficiently long exposure time and disappearance of the diffraction pattern, the irradiated areas look very dark for all incident

electron energies in bright-field images (Fig S4.6 in Supporting Information, Part D). This change in the irradiated regions is also reflected in the spectroscopic features, as described below.

In general, the number of electrons reflected from an area of the sample, and hence the image intensity, is a function of the incident electron energy. By plotting the intensity versus the incoming beam energy, we obtain an intensity-vs-voltage plot, or in short, a LEEM-IV curve. A LEEM-IV curve is a spectroscopic fingerprint of the probed area, and is largely determined by the unoccupied band-structure of the sample above the vacuum energy. [23,24] The reflected specular intensity is directly related to the density of states (DOS) in the solid along the surface normal. A low density of unoccupied states lowers the probability that incoming electrons enter the solid, resulting in higher reflectivity. Conversely, a high density of states leads to a low reflectivity. Fig. 4.4 shows LEEM-IV curves of a crystalline pentacene film, three monolayers in thickness, measured repeatedly on the same area. These LEEM-IV curves follow the intensity variations of the 0^{th}-order diffraction peak, corresponding to specularly-reflected electrons. After each subsequent measurement, the features of the LEEM-IV curve are diminished, meaning that a smaller fraction of the incident electrons undergo specular reflection. The latter is consistent with our previous result that irradiated areas appear gradually darker in real-space images. For an area exposed to the electron beam for a sufficiently long time, all the IV curve features are lost, as can be seen in Fig. 4.4. This indicates that the states associated with the original pentacene layer disappear, suggesting a new material with a broad set of unoccupied states is being formed. This is the reason irradiated areas appear very dark with no intensity change in bright-field real-space images obtained by incident electrons of any energy. In a related observation, the background intensity in diffraction images is noted to increase during irradiation (Fig. S4.7, Supporting Information, Part E), indicating that more electrons are scattered incoherently after a period of exposure to the beam.

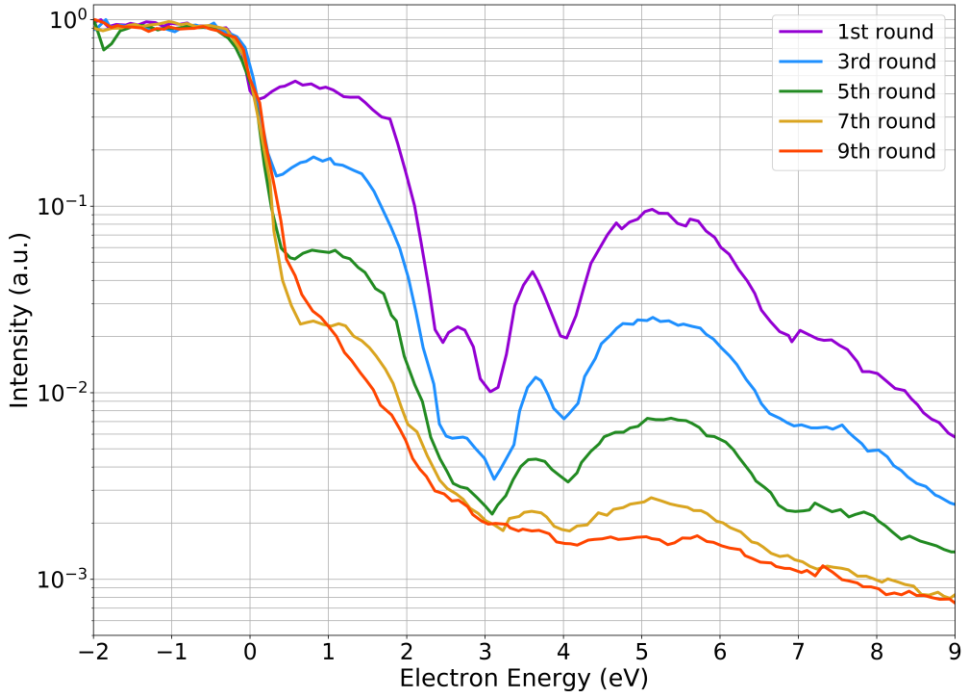

Fig. 4.4 Diminishing of LEEM-IV features through consecutive measurements. The LEEM-IV curves correspond to the intensity of the (0,0) diffraction peak of a sample with film thickness of 3 monolayers. The beam current density for the measurements is 5.3 pA/μm^2.

Finally, Fig. S4.8 (Supporting Information, Part F) shows the changes in the electron energy loss spectra after a period of exposure to the beam. It can be inferred that the energy distribution of the secondary electrons is such that the vast majority of them have an energy of less than ~4 eV. Considering our observations about the damage cross-section in pentacene layers, it can be concluded that the secondary electrons generated during irradiation contribute minimally to the damage cross-sections for the incident electron energies in our study.

4.4 Discussion

To analyze the full energy dependence of the damage cross-section curve depicted in Fig. 4.3, we consider possible mechanisms of interaction of molecules with incoming electrons having different energies. At few-eV incident energies, “electron attachment” is

regarded as the primary mechanism. It can lead to either auto-detachment of the electron, leaving the molecule in an excited state, or fragmentation of the molecule, i.e. the case of Dissociative Electron Attachment (DEA), or formation of reactive negatively-charged centers via rearrangement of charge within the molecule. The relative probability of each of these scenarios depends on the energetic landscape (potential energy surfaces) of the molecule. Electron attachment and formation of anions at low electron energies has been investigated with different techniques and reported for pentacene and similar molecules in the literature. In particular, mass-spectroscopic studies of vapors of pentacene molecules bombarded with low-energy electrons found that singly charged anions of pentacene could be detected for electron energies in the range 0-3 eV, demonstrating electron attachment at such energies. [31] In the same study, neutral pentacene molecules were detected, also up to 3 eV. In another similar mass-spectroscopic study [32], singly charged anions of pentacene molecules with one hydrogen missing were detected starting from ~ 5 eV, up to ~ 11 eV, with much smaller quantities (about 100 times lower) found in the range 3-5 eV. Singly charged negative anions of other polycyclic aromatic hydrocarbons with one hydrogen missing were also detected in several other studies [33,34], showing a distribution centered around 8 eV, and becoming increasingly smaller above 10 eV and below 6 eV. In a study of vibrational states of gaseous benzene molecules probed with incident electrons, the cross-section for excitation of the carbon-hydrogen bond is shown to have a resonance between 5.5 eV and 10 eV, with a peak at 8 eV, accompanied by a smaller resonance between 4 eV and 5.5 eV. [35] Electron bombardment of an aromatic thiol (Au-S-$CH_2C_6H_5$) was found to result in creation of H_2 molecules, with the yield becoming drastically smaller below ~6 eV. [36] Irradiation of p-terphenylthiol SAMs with LEEs was found to show a resonance centered at 7.2 eV for excitation of carbon-hydrogen bonds. [37,38]

From these results, we conclude that at energies in the range from 0 eV up to about 10 eV, the incoming electrons can attach to the pentacene molecules, however, towards the lower end of the range, the molecules most probably auto-detach the extra electron, and the temporary attachment is much less likely to lead to fragmentation of the molecule. Towards the upper end of the 0-10 eV range, electron attachment will leave the molecule in a chemically reactive state with consequences that are discussed further below. The new reactive state of the molecule can be a result of scission of the carbon-hydrogen bond and removal of a hydrogen atom from the molecule, charge reorganization after electron attachment or an energetically excited state after detachment of the electron. The increased resistance towards damage at very low electron energies is in contrast to results from similar LEEM experiments on PMMA and the molecular organometallic EUV resist known as tin-oxo cage [21,22], for both of which it was found that electrons with energies all the way

down to 0 eV (with respect to vacuum energy) can cause chemical changes in the resist layer. Lower susceptibility of aromatic organic molecules towards irradiation damage, compared to their derivatives which contain also single bonds, such as the case of pentacene and bis(triisopropylsilylethynyl) (TIPS) pentacene [39,40], or compared to saturated molecules [41], has already been reported in various studies. In agreement with our observations on pentacene layers, an Inverse Photo-Emission Spectroscopy (IPES) study on pentacene films also found no remarkable change in the spectra when electrons with kinetic energy of 5 eV were used, in contrast to the case for 10 eV electrons for which spectral changes were observed. [42]

As the incident energy of the electrons increases above a few eV, also other mechanisms for interaction between the incoming electrons and the pentacene molecules become possible. For pentacene molecules bombarded with electrons, a threshold of 6.6 eV has been experimentally measured for ionization of pi-electrons of pentacene [43–47], with more ionizations as the incident electron energy increases. [44] Ionization of sigma bonds in pentacene is identified to start at approximately 11 eV [44], with the ionization leading to scission of carbon-hydrogen bonds starting at 15.2 eV. [43] In a related study, the ionization cross-section in benzene shows a steep rise from incident electron energy of ~9 eV (the ionization threshold in benzene) up to around 100 eV. [48] Similar behavior is expected to be the case for pentacene but starting from a lower ionization threshold. The availability of more pathways for interaction between the incident electrons and the molecules is manifested in the continuous increase of the damage cross-section versus electron energy observed in Fig. 4.3. However, DEA is assumed to contribute to damage in pentacene mostly for electron energies below ~11 eV, given the diminished amounts of singly charged anions of pentacene molecules with one hydrogen missing detected at energies higher than ~11 eV, as found in Ref. [32]. Indeed, electron attachment and formation of a transient negative ion is expected to happen for electron energies below 15 eV. [1,2,49] At higher incident electron energies, impact ionization is expected to be the dominant interaction mechanism.

The cross-sections for damage to the pentacene crystal lattice obtained here are within the range of cross-sections reported in literature for interaction of electrons with gaseous benzene. [48,50–53] A lower damage cross-section for pentacene films could be expected due to higher irradiation damage resistance of pentacene compared to benzene, as a result of a higher degree of electron delocalization both within the molecule and also within the layer with neighboring molecules.

Irradiation with electrons has been reported in various studies to lead to cross-linking within the organic layer, such as the case of 4'-nitro-1,1´-biphenyl-4-thiol SAM (incident electron

energies 2.5-100 eV) [54], 1,1'-biphenyl-4-thiol (BPT) SAM (incident electron energy 50 eV) [55], $CH_3(C_6H_4)_2(CH_2)_nSH$ SAM (incident electron energy 10 eV) [56], and p-terphenylthiol SAMs (incident electron energies 6 eV and 50 eV). [37,57] Hence, we propose that the mechanism behind damage to the pentacene crystalline structure is formation of chemical bonds between nearby molecules initiated by reactive atoms. The reactive atoms are created either as a result of (dissociative) electron attachment at lower energies, or impact ionization at energies higher than thresholds for scission of various bonds. This process, repeated many times across the layer, will eventually result in polymerization of the molecular film, and creation of a CNM. At higher electron energies, scission of different bonds, fragmentation of molecules and drifting away of the fragments are also possible.

This conclusion is also compatible with the LEEM-IV measurements, presented in Fig. 4.4. In the first measurement, the LEEM-IV curve shows reflection maxima at about 2 and 5.5 eV, separated by a pronounced minimum (low reflectivity) at about 3.5 eV. As shown previously [23,24], high electron reflectivity corresponds to a gap in the electronic band structure, i.e. low density of states in the conduction band above the vacuum level. The disappearance of the reflection maxima at these energies with consecutive exposures indicates a loss of crystal order, and thereby a loss of electronic structure, including these bandgaps. Given that orbital energies are affected/-shifted corresponding to their environment, creation of a disordered CNM is expected to lead to a more dispersed set of energies for unoccupied orbitals. This in turn results in low reflectivity and featureless LEEM-IV curves for irradiated pentacene areas compared to pristine areas showing clear dips and peaks. Polymerization of the layers, resulting in a more rugged surface, also explains loss of definition in the real-space images upon irradiation, as well as the increase in the background intensity (noncoherent scattering) in diffraction images observed in Fig. S4.7.

4.5 Conclusions

Crystalline thin films consisting of 2-4 pentacene monolayers are grown on silicon substrates *in situ* in the UHV chamber of a low-energy electron microscope. It is observed that irradiation of the films with low-energy electrons leads to fading of their diffraction pattern at a rate that depends on the energy of the incident electrons. Cross-sections for damage to the crystalline structure of the thin films are obtained by analysis of the evolution of the diffraction peaks over time. The results indicate that the damage cross-section increases by more than an order of magnitude for electron energies from 0 eV to 10 eV, and by another order of magnitude from 10 eV to 40 eV. Spectroscopic LEEM-IV measurements also show

gradual disappearance of unoccupied band structure as a result of continued irradiation. These observations are explained by the different mechanisms that govern the interaction of pentacene molecules with incoming electrons having different energies. Electron attachment is proposed as the dominant mechanism at low energies, and a contributing factor to damage up to ~10 eV. It can lead to scission of carbon-hydrogen bonds and removal of hydrogen (with a higher likelihood above ~5 eV), or otherwise leave the molecule in a chemically reactive state. Impact ionization plays a bigger role as the energy of the electrons increases beyond various ionization thresholds. Scission of various other bonds and fragmentation of the molecule are assumed to happen at higher energies. The fading of the diffraction pattern and the spectroscopic LEEM-IV features is proposed to be a result of polymerization of the layer and its transformation into a CNM, triggered by scission of molecular bonds and creation of radicals. Loss of definition in real-space images and increase in background intensity in diffraction images also indicate a more disordered surface landscape, likely as a result of polymerization of the layer. From electron energy loss measurements, secondary electrons generated during exposure were found to have energies mostly below ~4 eV and, as a result, have a negligible contribution to the damage cross-sections.

The implications of these results should be taken into account in experiments and processes that expose organic samples and materials to low-energy electrons, in the form of either a primary beam or as secondaries produced upon exposure of the sample to high energy electrons or photons. Note that such secondaries would possess energies within the range studied here. Given the lower damage rate at few-eV incident electron energies, experiments can be designed such that the sample is not destroyed or lasts longer during the experiment. The results can also point to the possible use of aromatic systems as electron resists with a significant energy threshold, to reduce the effects of low-energy secondary electrons in resist exposure. This may reduce the sensitivity of the resist, but also improve resolution and line edge roughness.

References

[1] L. Sanche, *Low Energy Electron-Driven Damage in Biomolecules*, Eur. Phys. J. D **35**, 367 (2005).

[2] B. Boudaïffa, P. Cloutier, D. Hunting, M. A. Huels, and L. Sanche, *Resonant Formation of DNA Strand Breaks by Low-Energy (3 to 20 eV) Electrons*, Science **287**, 1658 (2000).

[3] A. W. Robertson, C. S. Allen, Y. A. Wu, K. He, J. Olivier, J. Neethling, A. I. Kirkland, and J. H. Warner, *Spatial Control of Defect Creation in Graphene at the Nanoscale*, Nat. Commun. **3**, 1144 (2012).

[4] U. Kaiser et al., *Transmission Electron Microscopy at 20kV for Imaging and Spectroscopy*, Ultramicroscopy **111**, 1239 (2011).

[5] J. R. Fryer, C. H. McConnell, F. Zemlin, and D. L. Dorset, *Effect of Temperature on Radiation Damage to Aromatic Organic Molecules*, Ultramicroscopy **40**, 163 (1992).

[6] K. Murata and M. Wolf, *Cryo-Electron Microscopy for Structural Analysis of Dynamic Biological Macromolecules*, BBA - General Subjects **1862**, 324 (2018).

[7] L. A. Baker and J. L. Rubinstein, *Radiation Damage in Electron Cryomicroscopy*, in *Methods in Enzymology*; Jensen, G. J., Ed.; Academic Press (2010); Vol. 481, pp 371−388

[8] B. E. Bammes, J. Jakana, M. F. Schmid, and W. Chiu, *Radiation Damage Effects at Four Specimen Temperatures from 4 to 100 K*, J. Struct. Biol. **169**, 331 (2010).

[9] S. T. Skowron, S. L. Roberts, A. N. Khlobystov, and E. Besley, *The Effects of Encapsulation on Damage to Molecules by Electron Radiation*, Micron **120**, 96 (2019).

[10] J. R. Fryer, *Molecular Arrays and Molecular Structure in Organic Thin Films Observed by Electron Microscopy*, J. Phys. D: Appl. Phys. **26**, B137 (1993).

[11] A. Turchanin, D. Käfer, M. El-Desawy, C. Wöll, G. Witte, and A. Gölzhäuser, *Molecular Mechanisms of Electron-Induced Cross-Linking in Aromatic SAMs*, Langmuir **25**, 7342 (2009).

[12] A. Turchanin and A. Gölzhäuser, *Carbon Nanomembranes*, Advanced Materials **28**, 6075 (2016).

[13] A. Turchanin, *Synthesis of Molecular 2D Materials via Low-Energy Electron Induced Chemical Reactions*, Chimia **73**, 473 (2019).

[14] X. Zhang, C. Neumann, P. Angelova, A. Beyer, and A. Gölzhäuser, *Tailoring the Mechanics of Ultrathin Carbon Nanomembranes by Molecular Design*, Langmuir **30**, 8221 (2014).

[15] P. Angelova et al., *A Universal Scheme to Convert Aromatic Molecular Monolayers into Functional Carbon Nanomembranes*, ACS Nano **7**, 6489 (2013).

[16] S. J. Noever et al., *Transferable Organic Semiconductor Nanosheets for Application in Electronic Devices*, Adv. Mater. **29**, 1606283 (2017).

[17] J. Li and F. Banhart, *The Engineering of Hot Carbon Nanotubes with a Focused Electron Beam*, Nano Lett. **4**, 1143 (2004).

[18] T. W. Chamberlain et al., *Stop-Frame Filming and Discovery of Reactions at the Single-Molecule Level by Transmission Electron Microscopy*, ACS Nano **11**, 2509 (2017).

[19] D. Ugarte, *Curling and Closure of Graphitic Networks under Electron-Beam Irradiation*, Nature **359**, 707 (1992).

[20] F. Banhart and P. M. Ajayan, *Carbon Onions as Nanoscopic Pressure Cells for Diamond Formation*, Nature **382**, 433 (1996).

[21] I. Bespalov, Y. Zhang, J. Haitjema, R. M. Tromp, S. J. van der Molen, A. M. Brouwer, J. Jobst, and S. Castellanos, *Key Role of Very Low Energy Electrons in Tin-Based Molecular Resists for Extreme Ultraviolet Nanolithography*, ACS Appl. Mater. Interfaces **12**, 9881 (2020).

[22] A. Thete, D. Geelen, S. J. van der Molen, and R. M. Tromp, *Charge Catastrophe and Dielectric Breakdown during Exposure of Organic Thin Films to Low-Energy Electron Radiation*, Phys. Rev. Lett. **119**, 266803 (2017).

[23] J. Jobst, J. Kautz, D. Geelen, R. M. Tromp, and S. J. van der Molen, *Nanoscale Measurements of Unoccupied Band Dispersion in Few-Layer Graphene*, Nat. Commun. **6**, 8926 (2015).

[24] J. Jobst, A. J. H. van der Torren, E. E. Krasovskii, J. Balgley, C. R. Dean, R. M. Tromp, and S. J. van der Molen, *Quantifying Electronic Band Interactions in van der*

Waals Materials Using Angle-Resolved Reflected-Electron Spectroscopy, Nat. Commun. **7**, 13621 (2016).

[25] R. M. Tromp, Y. Fujikawa, J. B. Hannon, A. W. Ellis, A. Berghaus, and O. Schaff, *A Simple Energy Filter for Low Energy Electron Microscopy/Photoelectron Emission Microscopy Instruments*, J. Phys.: Condens. Matter. **21**, 314007 (2009).

[26] S. M. Schramm, J. Kautz, A. Berghaus, O. Schaff, R. M. Tromp, and S. J. van der Molen, *Low-Energy Electron Microscopy and Spectroscopy with ESCHER: Status and Prospects*, IBM J. Res. & Dev. **55**, 1:1 (2011).

[27] F. J. Meyer zu Heringdorf, M. C. Reuter, and R. M. Tromp, *Growth Dynamics of Pentacene Thin Films*, Nature **412**, 517 (2001).

[28] F. J. Meyer Zu Heringdorf, M. C. Reuter, and R. M. Tromp, *The Nucleation of Pentacene Thin Films*, Appl. Phys. A **78**, 787 (2004).

[29] A. Al-Mahboob, J. T. Sadowski, Y. Fujikawa, K. Nakajima, and T. Sakurai, *Kinetics-Driven Anisotropic Growth of Pentacene Thin Films*, Phys. Rev. B **77**, 035426 (2008).

[30] M. Misra and R. F. Egerton, *Assessment of Electron Irradiation Damage to Biomolecules by Electron Diffraction and Electron Energy-Loss Spectroscopy*, Ultramicroscopy **15**, 337 (1984).

[31] R. V. Khatymov, R. F. Tuktarov, and M. V. Muftakhov, *Lifetime of Negative Molecular Ions of Tetracene and Pentacene with Respect to the Autodetachment of an Electron*, JETP Lett. **93**, 437 (2011).

[32] M. V. Muftakhov, R. V. Khatymov, and R. F. Tuktarov, *Decomposition of Aromatic Compounds Relevant to Organic Electronics under Exposure to Low-Energy Electrons*, Tech. Phys. **63**, 1854 (2018).

[33] I. Kh. Aminev, V. I. Khvostenko, V. P. Yur'ev, and G. A. Tolstikov, *Mass Spectra of Negative Ions of Condensed Aromatic Hydrocarbons and Biphenyl*, Russ. Chem. Bull. **22**, 1831 (1973).

[34] S. Tobita, M. Meinke, E. Illenberger, L. G. Christophorou, H. Baumgärtel, and S. Leach, *Polycyclic Aromatic Hydrocarbons: Negative Ion Formation Following Low Energy (0-15 eV) Electron Impact*, Chem. Phys. **161**, 501 (1992).

[35] R. Azria and G. J. Schulz, *Vibrational and Triplet Excitation by Electron Impact in Benzene*, J. Chem. Phys. **62**, 573 (1975).

[36] P. Rowntree, P. C. Dugal, D. Hunting, and L. Sanche, *Electron Stimulated Desorption of H_2 from Chemisorbed Molecular Monolayers*, J. Phys. Chem. **100**, 4546 (1996).

[37] L. Amiaud, J. Houplin, M. Bourdier, V. Humblot, R. Azria, C. M. Pradier, and A. Lafosse, *Low-Energy Electron Induced Resonant Loss of Aromaticity: Consequences on Cross-Linking in Terphenylthiol SAMs*, Phys. Chem. Chem. Phys. **16**, 1050 (2014).

[38] J. Houplin, L. Amiaud, C. Dablemont, and A. Lafosse, *DOS and Electron Attachment Effects in the Electron-Induced Vibrational Excitation of Terphenylthiol SAMs*, Phys. Chem. Chem. Phys. **17**, 30721 (2015).

[39] J. Chen, D. C. Martin, and J. E. Anthony, *Morphology and Molecular Orientation of Thin-Film Bis(Triisopropylsilylethynyl) Pentacene*, J. Mater. Res. **22**, 1701 (2007).

[40] A. S. Eggeman, S. Illig, A. Troisi, H. Sirringhaus, and P. A. Midgley, *Measurement of Molecular Motion in Organic Semiconductors by Thermal Diffuse Electron Scattering*, Nat. Mater. **12**, 1045 (2013).

[41] L. E. Firment and G. A. Somorjai, *Surface Structures of Normal Paraffins and Cyclohexane Monolayers and Thin Crystals Grown on the (111) Crystal Face of Platinum. A Low-energy Electron Diffraction Study*, J. Chem. Phys. **66**, 2901 (1977).

[42] W. Han, H. Yoshida, N. Ueno, and S. Kera, *Electron Affinity of Pentacene Thin Film Studied by Radiation-Damage Free Inverse Photoemission Spectroscopy*, Appl. Phys. Lett. **103**, 123303 (2013).

[43] H. W. Jochims, H. Baumgärtel, and S. Leach, *Structure-Dependent Photostability of Polycyclic Aromatic Hydrocarbon Cations: Laboratory Studies and Astrophysical Implications*, ApJ **512**, 500 (1999).

[44] M. S. Deleuze, A. B. Trofimov, and L. S. Cederbaum, *Valence One-Electron and Shake-up Ionization Bands of Polycyclic Aromatic Hydrocarbons. I. Benzene, Naphthalene, Anthracene, Naphthacene, and Pentacene*, J. Chem. Phys. **115**, 5859 (2001).

[45] R. Boschi, J. N. Murrell, and W. Schmidt, *Photoelectron Spectra of Polycyclic Aromatic Hydrocarbons*, Faraday Discuss. Chem. Soc. **54**, 116 (1972).

[46] R. Boschi, E. Clart, and W. Schmidt, *Photoelectron Spectra of Polynuclear Aromatics. III. the Effect of Nonplanarity in Sterically Overcrowded Aromatic Hydrocarbons*, J. Chem. Phys. **60**, 4406 (1974).

[47] W. Schmidt, *Photoelectron Spectra of Polynuclear Aromatics. V. Correlations with Ultraviolet Absorption Spectra in the Catacondensed Series*, J. Chem. Phys. **66**, 828 (1977).

[48] W. Hwang, Y. K. Kim, and M. E. Rudd, *New Model for Electron-Impact Ionization Cross Sections of Molecules*, J. Chem. Phys. **104**, 2956 (1996).

[49] C. R. Arumainayagam, H. L. Lee, R. B. Nelson, D. R. Haines, and R. P. Gunawardane, *Low-Energy Electron-Induced Reactions in Condensed Matter*, Surf. Sci. Rep. **65**, 1 (2010).

[50] C. I. M. Beenakker and F. J. de Heer, *Dissociative Excitation of Benzene by Electron Impact*, Chem. Phys. Lett. **29**, 89 (1974).

[51] P. Mozejko, G. Kasperski, C. Szmytkowski, G. P. Karwasz, R. S. Brusa, and A. Zecca, *Absolute Total Cross Section Measurements for Electron Scattering on Benzene Molecules*, Chem. Phys. Lett. **257**, 309 (1996).

[52] H. Kato, M. C. Garcia, T. Asahina, M. Hoshino, C. Makochekanwa, H. Tanaka, F. Blanco, and G. García, *Absolute Elastic Differential Cross Sections for Electron Scattering by $C_6H_5CH_3$ and $C_6H_5CF_3$ at 1.5-200 eV: A Comparative Experimental and Theoretical Study with C_6H_6*, Phys. Rev. A **79**, 062703 (2009).

[53] H. Kato, M. Hoshino, H. Tanaka, P. Limo-Vieira, O. Inglfsson, L. Campbell, and M. J. Brunger, *A Study of Electron Scattering from Benzene: Excitation of the $^1B_{1u}$, $^3E_{2g}$, and $^1E_{1u}$ Electronic States*, J. Chem. Phys. **134**, 134308 (2011).

[54] C. Neumann, R. A. Wilhelm, M. Küllmer, and A. Turchanin, *Low-Energy Electron Irradiation Induced Synthesis of Molecular Nanosheets: Influence of the Electron Beam Energy*, Faraday Discuss. **227**, 61 (2021).

[55] W. Geyer, V. Stadler, W. Eck, M. Zharnikov, A. Gölzhäuser, and M. Grunze, *Electron-Induced Crosslinking of Aromatic Self-Assembled Monolayers: Negative Resists for Nanolithography*, Appl. Phys. Lett. **75**, 2401 (1999).

[56] S. Frey, H. T. Rong, K. Heister, Y. J. Yang, M. Buck, and M. Zharnikov, *Response of Biphenyl-Substituted Alkanethiol Self-Assembled Monolayers to Electron Irradiation: Damage Suppression and Odd-Even Effects*, Langmuir **18**, 3142 (2002).

[57] J. Houplin, C. Dablemont, L. Sala, A. Lafosse, and L. Amiaud, *Electron Processing at 50 eV of Terphenylthiol Self-Assembled Monolayers: Contributions of Primary and Secondary Electrons*, Langmuir **31**, 13528 (2015).

Supporting Information

Part A: Filtering procedure to remove the background from diffraction images

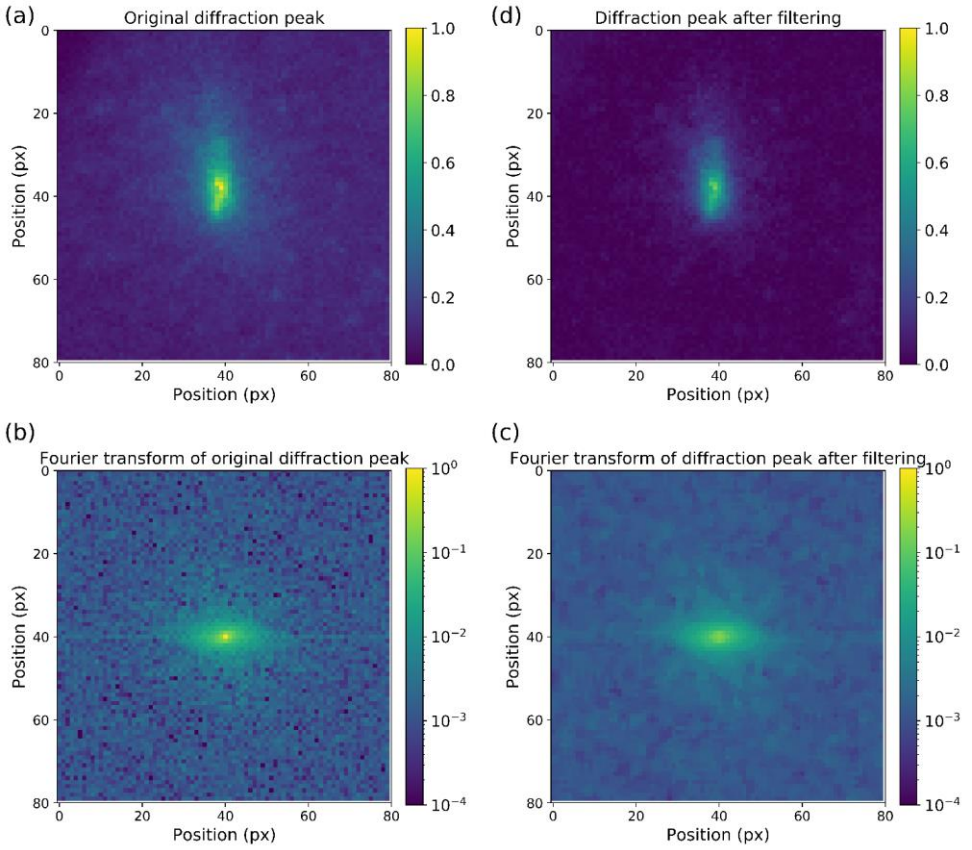

Fig. S4.1 A median filter is applied to the Fourier transform of each diffraction image to remove the low-frequency noise and background. (a) a measured diffraction peak, (b) Fourier transform of the diffraction peak, (c) median filter applied to (b), (d) inverse Fourier transform of (c). The original and filtered images are normalized to the same value, for both the top and the bottom pairs.

Part B: Damage cross-sections of more samples

Damage cross-sections of (0,0) diffraction peak measured with different beam currents on samples with pentacene film thicknesses of 2-4 monolayers.

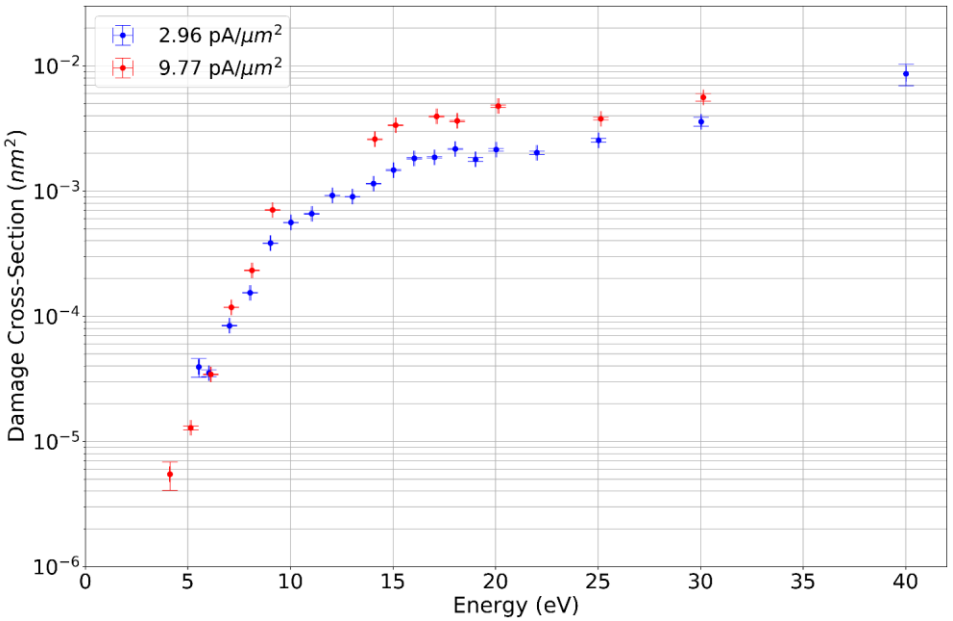

Fig. S4.2 Damage cross-sections of (0,0) diffraction peak versus incident electron energy, measured with two different electron beam currents on the same sample with film thickness of 4 monolayers.

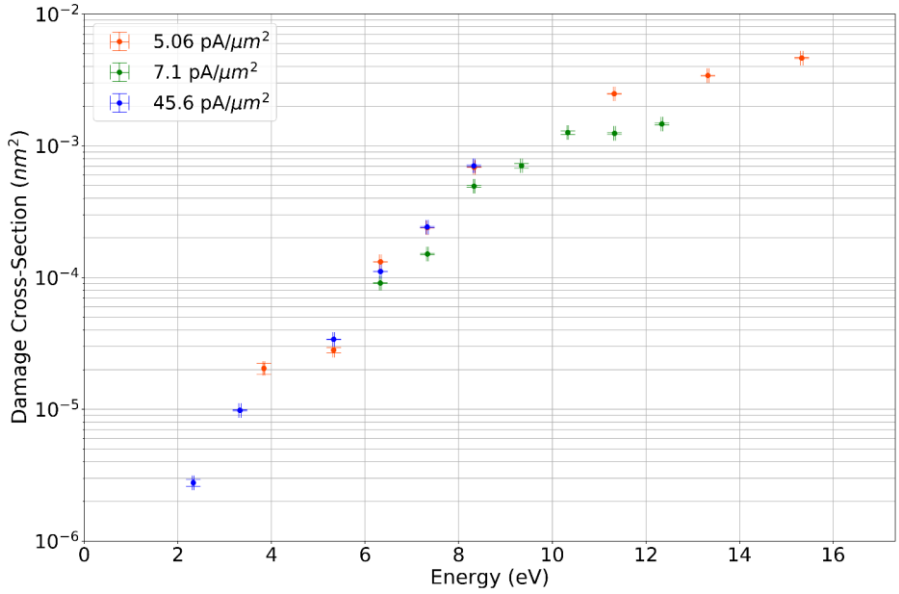

Fig. S4.3 Damage cross-sections of (0,0) diffraction peak versus incident electron energy measured with different electron beam currents. Datasets with beam current densities 45.6 pA/μm^2 and 5.06 pA/μm^2 belong to the same sample. The dataset with beam current density 7.1 pA/μm^2 belongs to a different sample. Both samples have a film thickness of 3 monolayers.

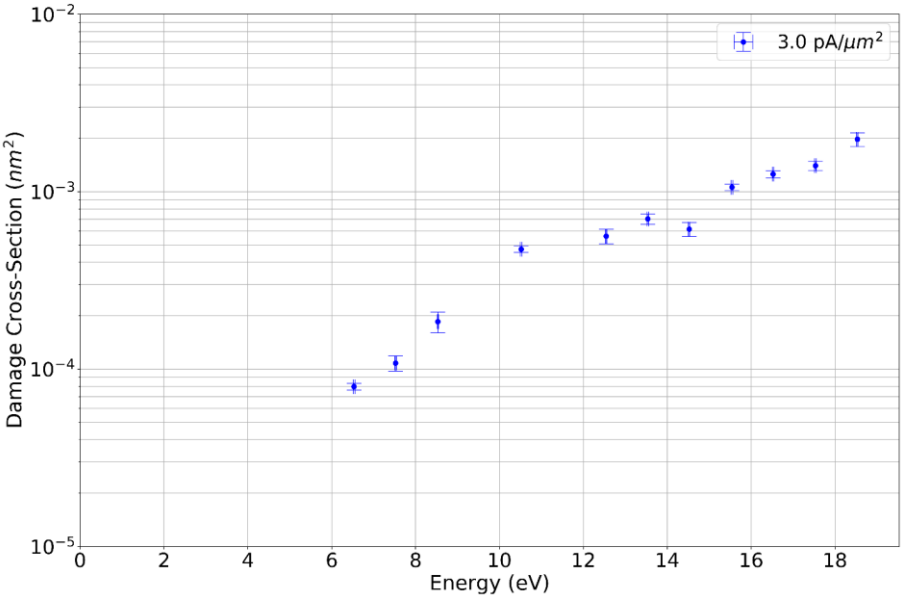

Fig. S4.4 Damage cross-sections of (0,0) diffraction peak versus incident electron energy measured on a sample with pentacene film thickness of 2 monolayers.

Part C: Evolution of widths of Lorentzian fits during irradiation

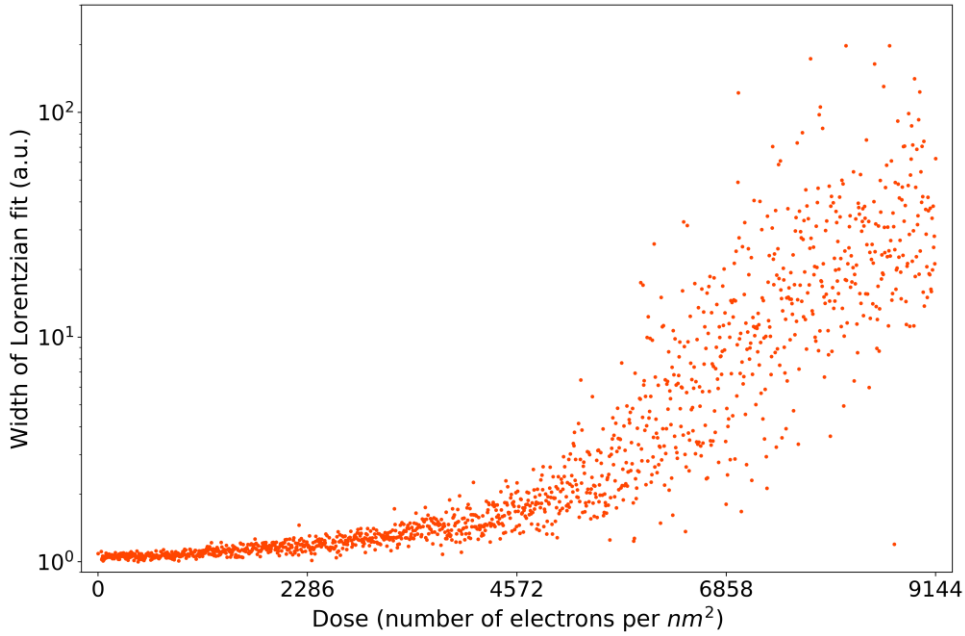

Fig. S4.5 Evolution of widths of Lorentzian fits to line profile of a (1,1) diffraction peak during irradiation with 10 eV electrons. The thickness of pentacene film is 4 monolayers and the beam current density is 2.96 pA/μm^2. This figure is obtained from the same recording as Fig. 4.2

Part D: Irradiation damage in real-space images

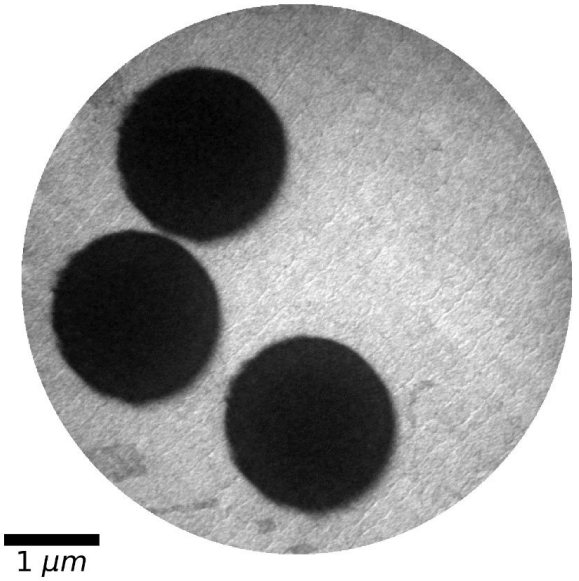

Fig. S4.6 Bright-field LEEM image of a sample with film thickness of 4 monolayers, obtained with electron energy 3.8 eV. The regions selected by an illumination aperture for damage recordings appear dark after irradiation with 16 eV, 14 eV and 12 eV electrons, respectively, from top to bottom.

Part E: Increase of background intensity in diffraction images due to irradiation

The figures below show the percentage of intensity change for all pixels across the entire diffraction image for the last few frames at the end of a period of exposure compared to the beginning. The images show an increase in the background intensity and a decrease in the intensity around the diffraction spots, indicating that more electrons are scattered incoherently.

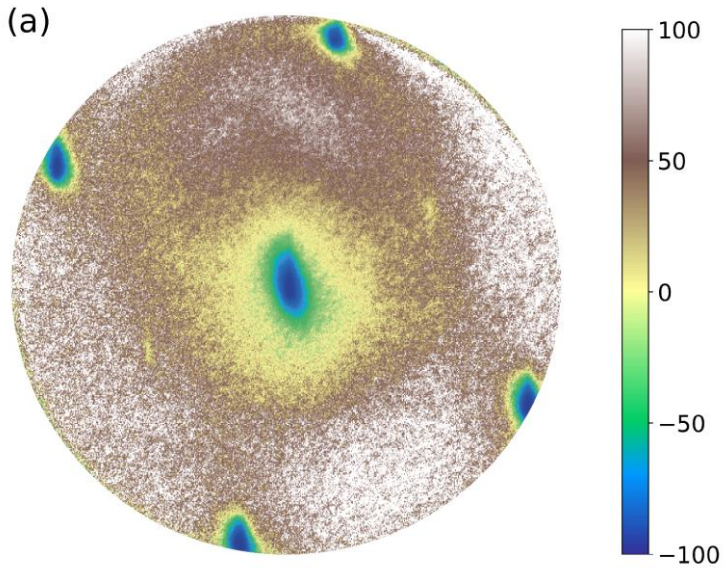

Fig. S4.7 (a) Percentage of change in intensity for all pixels across the diffraction image. The intensity of the last few frames at the end of a period of irradiation is compared with the first few frames. Intensity changes in regions with white color exceed 100%. Thickness of the pentacene film is 4 monolayers. Energy of incident electrons is 8 eV. The beam current density is 2.96 pA/μm^2

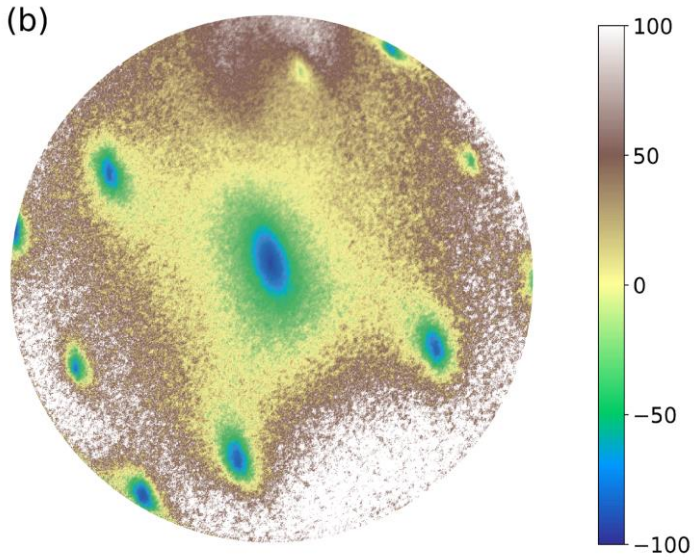

Fig. S4.7 (b) Percentage of change in intensity for all pixels across the diffraction image. The intensity of the last few frames at the end of a period of irradiation is compared with the first few frames. Intensity changes in regions with white color exceed 100%. Thickness of the pentacene film is 4 monolayers. Energy of incident electrons is 16 eV. The beam current density is 2.96 pA/μm^2

Part F: Changes in Electron Energy Loss Spectra due to irradiation

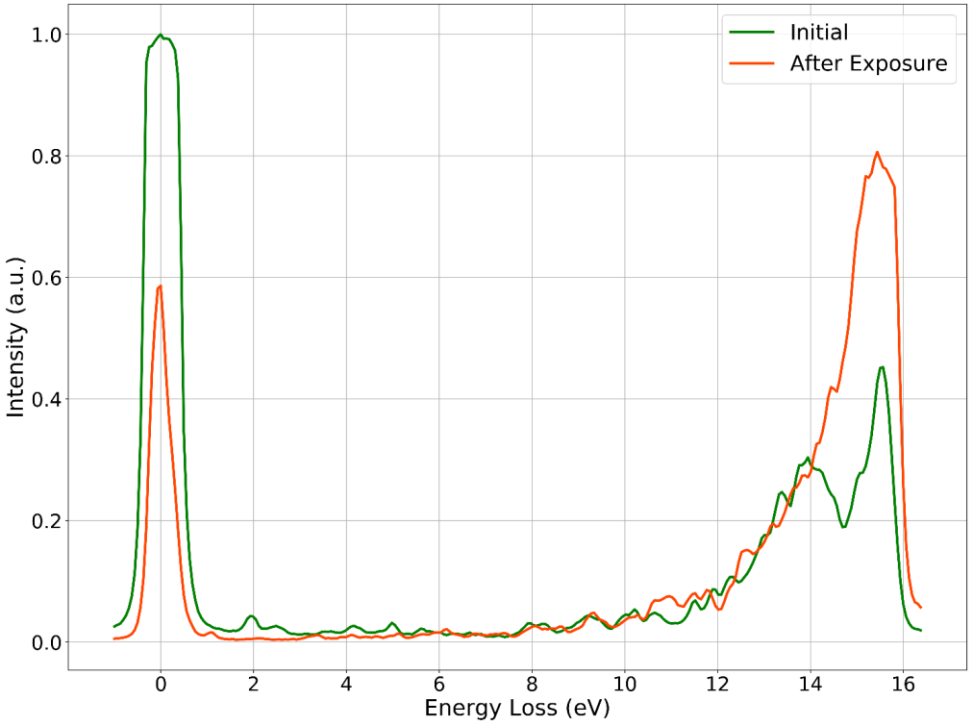

Fig. S4.8 Changes in the Electron Energy Loss Spectra of a sample with film thickness of 3 monolayers after a period of irradiation with electron energy 16.4 eV. The peak at 0 eV is the original beam, i.e. the (0,0) diffraction peak. The peak around 14 eV visible in the initial spectrum is due to excitation within the layer caused by the electrons. The peak at the end of the loss spectrum is associated with secondary electrons. This peak increases in intensity during irradiation.

Part G: Irradiation experiment on a HOPG flake

Similar irradiation experiments on a HOPG flake yield a negligible decay of intensity of diffraction peaks for the same electron doses. Fig. S4.9 shows a representative result for 7-eV electrons. Intensity fluctuations in Fig. S4.9 (especially for the HOPG sample) are attributed to electron beam fluctuations. This result rules out carbon deposition from the background pressure as being responsible for the decay of intensity of the diffraction spots of pentacene.

The HOPG flakes were exfoliated in ambient conditions on a silicon substrate, and subsequently transferred inside the microscope and heated (at UHV pressure of 1.0×10^{-9} mbar or better) at $500^{\circ C}$ for many hours to be cleaned.

Exposure measurements were carried out at room temperature, similar to measurements on pentacene samples.

Note again that both the growth of pentacene layers and the measurements on them are carried out in a UHV pressure of ~1.0×10^{-9} mbar or lower to ensure a clean environment for our experiments.

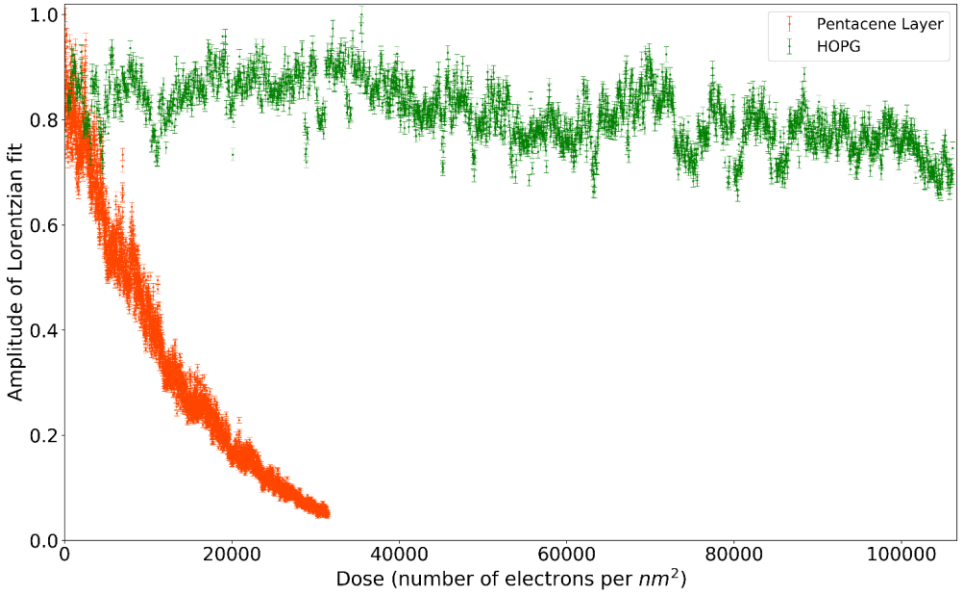

Fig. S4.9 Evolution of amplitudes of Lorentzian fits to 0^{th}-order diffraction spot for an HOPG flake compared to a pentacene film upon irradiation with 7 eV electrons. The pentacene film is four-monolayers in thickness. The beam current density is 2.96 pA/μm^2 for the pentacene sample and 16.1 pA/μm^2 for the HOPG sample.